Article

Analysis of Improved In-Cylinder Combustion Characteristics with Chamber Modifications of the Diesel Engine

Arun Teja Doppalapudi [1], Abul Kalam Azad [1,]*[ID] and Mohammad Masud Kamal Khan [2]

[1] School of Engineering and Technology, Central Queensland University, Melbourne Campus, 120 Spencer Street, Melbourne, VIC 3000, Australia
[2] School of Engineering, Computer and Mathematical Sciences, Auckland University of Technology, Auckland 1010, New Zealand
* Correspondence: azad.cqu@gmail.com or a.k.azad@cqu.edu.au

Abstract: This study numerically analyses the effects of chamber modifications to investigate the improvement of in-cylinder combustion characteristics of the diesel engine using a computational fluid dynamics (CFD) approach. Five different modified chambers, namely, the double swirl combustion chamber (DSCC), bathtub combustion chamber (BTCC), double toroidal re-entrant combustion chamber (DTRCC), shallow depth combustion chamber (SCC), and stepped bowl combustion chamber (SBCC) were developed and compared with a reference flat combustion chamber (FCC). The effects of chamber modifications on temperature formation, velocity distribution, injection profiles, and in-cylinder turbulent motions (swirl and tumble ratio) were investigated. During the compression stroke, near top dead centre, the SCC showed a peak temperature of 970 K, followed by the FCC (968 K), SBCC (967 K), and DTRCC (748 K to 815 K). The DSCC and the SCC showed a high swirl ratio above 0.6, whereas the DTRCC and the BTCC showed a high tumble ratio of approximately 0.4. This study found that the SCC, BTCC, and DSCC have better combustion rates than the FCC in terms of temperature, heat release rate, and velocity distribution. However, the DTRCC showed poor temperature formation rates and rapid heat release rates (approx. 150 J/°CA), which can lead to rapid combustion and knocking tendencies. In conclusion, the DSCC and the SCC showed better combustion rates than the other chambers. In addition, turbulent motions inside the chambers avoided combustion in crevice regions. This study recommends avoiding chambers with wider bowls in order to prevent uneven combustion across the cylinder. Furthermore, split bowls such as the DSCC, along with adjusted injection rates, can provide better results in terms of combustion.

Keywords: combustion chamber modification; combustion simulation; heat release rate; cylinder temperature; CFD analysis

1. Introduction

Air–fuel mixture formation inside the engine cylinder is mainly responsible for engine performance and emissions [1]. With the improper mixture, fuel accumulation can occur inside the chamber due to an uneven distribution of air and fuel, which can cause incomplete combustion. To address these issues, engine modifications such as nozzle modifications [2] and port flow design have been investigated during recent decades to improve the overall in-cylinder combustion [3–5]. In addition, injection modifications [6] and piston bowl modifications [7] have been experimentally investigated to improve the combustion behaviour of diesel engines. Among these, the piston bowl modification technique is well-documented in the literature as one good active technique that directly affects air–fuel mixture formation.

Piston bowl modifications have gained significant attention in the last decade due to their active interactions inside the cylinder during the air–fuel mixture formation [8]. The piston bowl influences the air–fuel mixture through turbulence, which is governed by

swirl and tumble motions. Wall-wetting and the formation of fuel pockets can be avoided using chamber modifications. Biodiesel tends to form fuel pockets inside the chamber as biodiesel viscosity is higher than diesel fuel [9–12]. Moreover, biodiesel is proven as the prospective replacement for diesel fuel to reduce greenhouse gas emissions [13–17]. Several experimental results have shown increased engine performance and combustion with piston bowl geometry modifications using biodiesel as a fuel. For instance, Jaichandar and Annamalai [18,19] and Jaichandar et al. [20] conducted an experimental analysis with combustion chamber modifications on different piston bowl geometries. The study reported that the modified toroidal re-entrant combustion chamber (TRCC) showed improved combustion characteristics, reduced fuel consumption, and increased thermal efficiency compared with the conventional test engine chamber, the Hemispherical combustion chamber (HCC). In addition, Channappagoudra et al. [21] conducted an experimental analysis with the TRCC, HCC, Straight Sided Piston Bowl Geometry (SSPBG), and TCC. The study reported that the TRCC showed better results than the others because of improved fuel atomisation, increased cylinder temperature, and high turbulent kinetic energy. However, these experimental studies do not provide a detailed understanding of the effects of chamber modifications on air–fuel mixture formation and combustion rates.

Optical and computational studies have helped to understand in-cylinder flow fields with respect to modified geometries and operating parameters. Optical studies have allowed researchers to understand flame movements, flow patterns, and combustion evolution [22]. On the other hand, computational studies have assisted in developing new design geometries. They helped to investigate the in-cylinder fluid flow behaviour with respect to the chambers, along with the engine characteristics and emission estimations. Previous simulation studies have described the chamber modifications based on injection behaviour. For instance, Li et al. [23] proposed a double swirl combustion chamber (DSCC) where the injected fuel splits in the chamber grooves and spreads towards the squish and bowl region. Later, Li et al. [24] introduced a lateral swirl combustion chamber (LSCS) to accommodate the fuel inside the chamber, so the combustion occurs near the bowl region. These studies have indicated better combustion with the modified chambers with reduced soot emissions. However, the thermal profile of the combustion chamber has not been explained clearly enough to understand the intrinsic role of modified chambers. Furthermore, modified chambers greatly support low-temperature combustion (LTC) engines [25,26] and dual-fuel engines [27,28]. For example, Han et al. [29] analysed a longer air–fuel mixture period formed in the swirl direction due to the bowl chamber, which led to low-temperature combustion.

In the past few decades, several experimental studies have been conducted on piston bowl modifications, suggesting that the bowl chamber has influenced engine characteristics such as engine performance and emissions [30–33]. However, very few studies have focused on investigating flow combustion behaviour inside the chamber in relation to bowl modifications [30,34,35]. Hence, the novelty of this study is to examine and analyse combustion behaviour with respect to different combustion chamber modifications. This study used a CFD approach to investigate the combustion regime by analysing in-cylinder temperature and velocity profiles. In addition, to investigate rapid combustion and heat release rates, multiple injection pulses were used for all piston bowl geometries.

The scope of this study was to investigate flow parameters inside the chamber with respect to chamber modifications. This study considered six different bowl chambers and performed the simulation at set operating conditions to evaluate key results from the modified chambers. The following section explains our simulation modelling methodology, along with the designs of different chamber profiles. Furthermore, this study presents critical results and discusses the effect of chamber modifications on cylinder compression rates, temperature, and velocity profiles with respect to crank angles. Finally, the study's conclusions and recommendations are presented.

2. Methodology

The combustion sector simulation was carried out with Ansys IC engine fluent tool. Firstly, a flat combustion chamber was prepared similar to the Kubota V3300 engine model by maintaining the engine's bore, stroke, compression ratio, and displacement. Figure 1 presents the process flowchart for engine simulation. The simulation methodology contains three main parts—geometry preparation, simulation, and post-processing. Geometry preparation is essential to fluid volume extraction and meshing. Data related to valve positions, valve seats, port alignments, and positions were gathered and accommodated in preparing the combustion chamber. Later, the chamber was updated with respect to fluid extraction and meshing errors. A computational mesh was created to calculate the results at each time step [36]. The input variables and initialisation process were carried out during the simulation setup, and the analysis was performed during the post-processing stage. Later, bowl shapes were designed by adjusting the clearance volume to maintain the engine compression ratio and displacement. A detailed explanation of these stages is explained in the following sections.
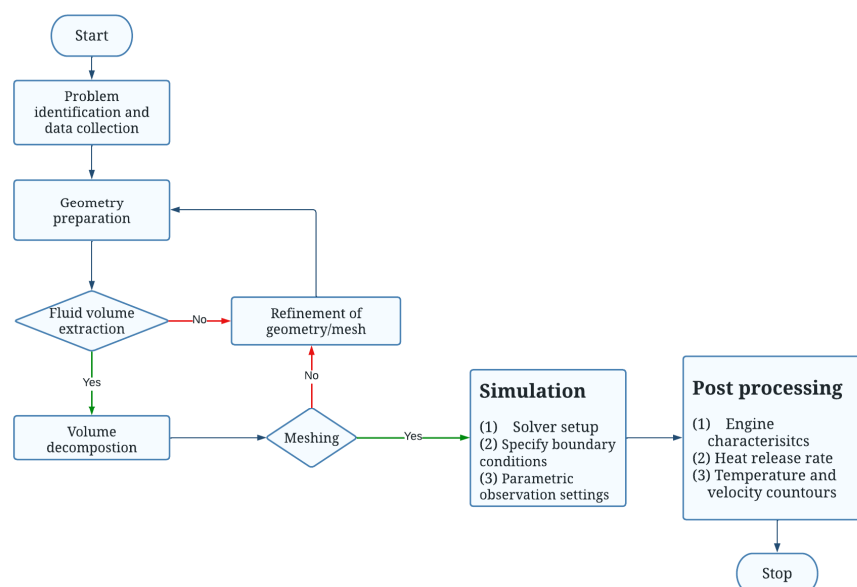

Figure 1. Flowchart for modelling and simulation of the engine.

2.1. Geometry Preparation and Meshing

In this simulation, the geometry was prepared based on the Kubota V3300 engine, as shown in Figure 2a. The detailed engine specifications are listed in Table 1. The Kubota V3300 engine is a four-cylinder heavy-duty tractor engine with two inlet valves and one exhaust valve. Moreover, it has a pre-chamber, where the combustion takes place in a separate combustion chamber and, from there, combusted gases travel to the main chamber. The modelling experiments were carried out on this Kubota V3300, a four-cylinder, four-stroke, compression ignition engine. The engine has a bore of 98 mm, a stroke of 110 mm, and a compression ratio of 22.6:1. The simulation was conducted at a speed of 1500 rpm.

A combustion chamber was created with two inlet valves and ports, and one exhaust valve and port. The cylinder displacement volume and pre-chamber rates were calculated, categorised, maintained, and modelled as direct injection engines. Arbitrary dimensions of the chamber components, such as valve heights and cylinder thickness, were assumed for the fluid extraction part as these have negligible impact on the combustion process. The fluid volume of the chamber was extracted by removing all the solid components except the valves, as shown in Figure 2b. A sector adaptive combustion simulation was carried out with an angle of 60°. The decomposed sector component of the cylinder chamber is presented in Figure 2c. During the decomposition process, the valve sets were deleted; the engine port was divided into a given sector angle of 60°; and the clearance volume and

crevice were adjusted with respect to the compression ratio, as shown in Figure 2c. In the next stage, adaptive refinement technology was used to generate the mesh for the model. Figure 2d presents the mesh component of a sector of a flat combustion chamber.
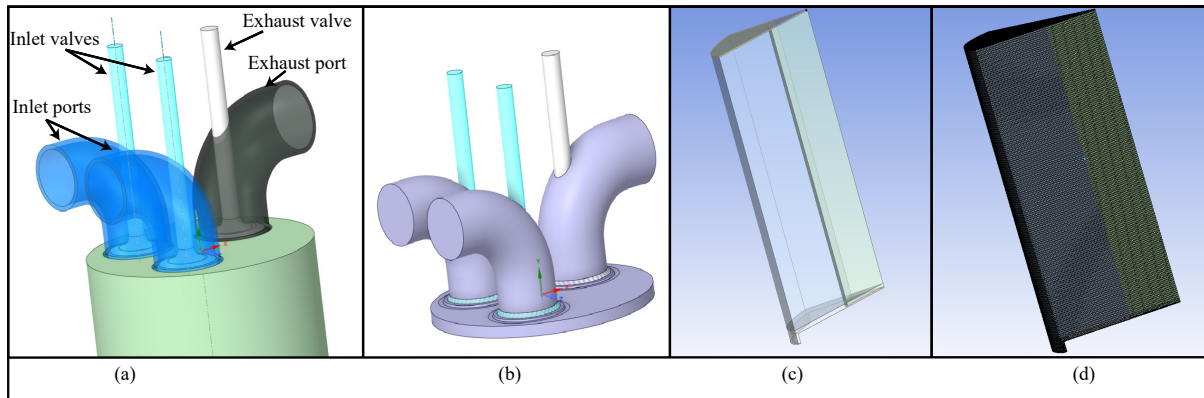

Figure 2. Geometry setup: (**a**) chamber with inlet and exhaust valves and ports; (**b**) fluid volume body; (**c**) 60° decomposed sector geometry; (**d**) meshing grid for sector geometry.

Table 1. Engine Specifications.

Make	Kubota V3300
Engine type	Vertical, 4-cycle liquid cooled diesel
Total displacement	3.318 (litres)
Fuel	Diesel surrogate (n-heptane)
Bore	98 mm
Stroke	110 mm
Compression ratio	22.6:1
Speed	1500 rpm
Fuel	Diesel
Cooling system	Water-cooled

2.2. Simulation Setup and Post-Processing

Ansys IC engine fluent software was used to conduct computational fluid dynamics (CFD) analysis. It provides an integrated environment with capabilities to set up powerful IC engine designs. Modelling an internal combustion engine involves dynamic interactions between moving geometries, fuel injection, and combustion processes. CFD involves jet formation, wall impingements, and combustion. The governing equations for the CFD analysis follow Navier–Stokes equations, which include conservation of energy, momentum, and continuity equations [37,38]. The governing equations are as follows.

The continuity equation:

$$\underbrace{\frac{\partial \rho}{\partial t}}_{material\ derivative} + \underbrace{\nabla(\rho V)}_{convective\ acceleration} = 0 \tag{1}$$

where ρ denotes the density of the fluid and V is the flow velocities in m/s.

The energy equation:

$$\frac{\partial(\rho e)}{\partial t} + \underbrace{\nabla(\rho e V)}_{kinetic\ energy} = \underbrace{\frac{\partial}{\partial x}\left(k\frac{\partial T}{\partial x}\right) + \frac{\partial}{\partial y}\left(k\frac{\partial T}{\partial y}\right)}_{conductive\ term} \tag{2}$$

Here, 'e' refers to the internal energy, k indicates the thermal conductivity, and T is the temperature.

The momentum equation (2-Dimensional):

$$\underbrace{\frac{\partial(\rho u)}{\partial t} + \frac{\partial\left(\rho u^2\right)}{\partial x} + \frac{\partial(\rho uv)}{\partial y}}_{inertia\ force} = \underbrace{-\frac{\partial(p)}{\partial x}}_{pressure\ gradient} +$$
$$\underbrace{\frac{\partial}{\partial x}\left(\lambda\left(\frac{\partial v}{\partial x} + \frac{\partial u}{\partial y}\right)V + 2\mu\frac{\partial u}{\partial x}\right) + \frac{\partial}{\partial y}\left(\mu\left(\frac{\partial v}{\partial x} + \frac{\partial u}{\partial y}\right)\right)}_{viscous\ force} \tag{3}$$

$$\frac{\partial(\rho v)}{\partial t} + \frac{\partial\left(\rho v^2\right)}{\partial y} + \frac{\partial(\rho uv)}{\partial x} = -\frac{\partial(p)}{\partial y} + \frac{\partial}{\partial x}\left(\mu\left(\frac{\partial v}{\partial x} + \frac{\partial u}{\partial y}\right)\right) + \frac{\partial}{\partial y}\left(\lambda\nabla V + 2\mu\left(\frac{\partial v}{\partial x}\right)\right) \tag{4}$$

Here, u and v are velocity magnitudes in the x and y directions, λ and μ are the shear stress (viscous effect) and dynamic viscosity, and p indicates pressure in Pascals.

The empirical k-ε model was used in this simulation. The turbulent motions inside the chamber were analysed using the Renormalization Group (RNG) k-ε model based on Reynolds averaged Navier–Stokes equations. The study adopted the RNG k-ε turbulent model to couple the stream fields and converge the solution into a continuity equation. This two-equation model statistically averages the multiscale eddies that are formed during combustion and can capture the horizontal velocity profiles along the free-flow streams. The turbulent kinetic energies (k) and the dissipation rates (ε) of these eddies are calculated using k-ε model [38,39].

To observe the turbulent kinetic energy (k):

$$\frac{\partial(\rho k)}{\partial t} + \frac{\partial(\rho k\mu_i)}{\partial x_i} = \frac{\partial}{\partial x_j}\left[\frac{\mu_i}{\sigma_k}\frac{\partial k}{\partial t}\right] + 2\mu_t E_{ij}E_{ij} - \rho\varepsilon \tag{5}$$

To observe the dissipation rate (ε):

$$\frac{\partial(\rho\varepsilon)}{\partial t} + \frac{\partial(\rho\varepsilon\mu_i)}{\partial x_i} = \frac{\partial}{\partial x_j}\left[\frac{\mu_t}{\sigma_e}\frac{\partial\varepsilon}{\partial x_j}\right] + C_{1\varepsilon}\frac{\varepsilon}{k}2\mu_t E_{ij}E_{ij} - C_{2\varepsilon}\rho\frac{\varepsilon^2}{k} \tag{6}$$

Apart from these, the Kelvin–Helmholtz (KH) instability model was used to predict the primary break-up model. A sector grid with periodic boundaries was adopted in this closed study from intake valve opening to exhaust valve closing. Dynamic mesh parameters, boundary conditions, materials, monitor setup, and relaxation factors were assigned during the simulation setup and initialised the solution.

The simulation setup procedure and boundary conditions were kept the same for all the piston bowl chambers. The simulation was conducted from the inlet valve closing period to the exhaust valve opening period. A constant swirl number of 1.3 was given to the inlet profiles with an injection angle of 70°. The injection was given with respect to the crank angle degree of 344 °CA to 370 °CA, as shown in Figure 3a. As represented in Figure 3b, the injection was provided with mass flow rates at three different intervals as pilot, main, and post injections. The natural atmospheric air composition was added as the intake air, and the cylinder walls were assigned to 440 K. The engine speed was kept constant at 1500 rpm.

Monitor definitions were created at the chamber bottom, chamber top and chamber fluid portion of the different cut planes. Max-vel-monitor was created to observe the maximum velocity, vol-avg-temp-monitor was created to observe the volume integral of temperature. During the post-processing stage, the results were recorded with respect to the monitor definitions according to the assigned cut planes. Before initialisation, the model setup, mixture formation, dynamic meshing, injections solution methods and solution controls were adjusted to solve the simulation. To verify the discretised equations, the convergence criteria for the velocity, k and ε were set to 1×10^{-4}, and energy was set to 1×10^{-6} with over 1400 iterations.
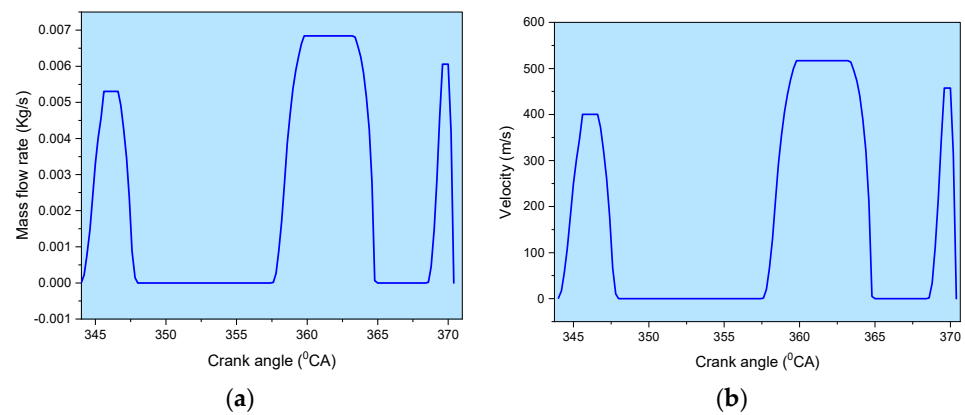
Figure 3. Fuel injection profiles: (**a**) injected fuel mass vs. °CA; (**b**) injected fuel velocity vs. °CA.

2.3. Grid Sensitivity Analysis

A computational grid independence study was performed for the FCC chamber to analyse the impact of the mesh grid on the simulation process. Firstly, a finer mesh was created with a reference mesh size of 0.611 and with five inflation layers. The fine mesh created 1,948,328 nodes and 1,878,444 elements. Similarly, the coarser mesh was created with a reference mesh size of 0.917 and with three inflation layers. The coarse mesh generated 597,824 nodes and 566,470 elements. Figure 4 presents the apparent heat release rate for the fine and coarse mesh. It can be seen from Figure 4 that the type of mesh used has a slight impact on the simulation results. Hence, the study progressed with the finer mesh attributes.
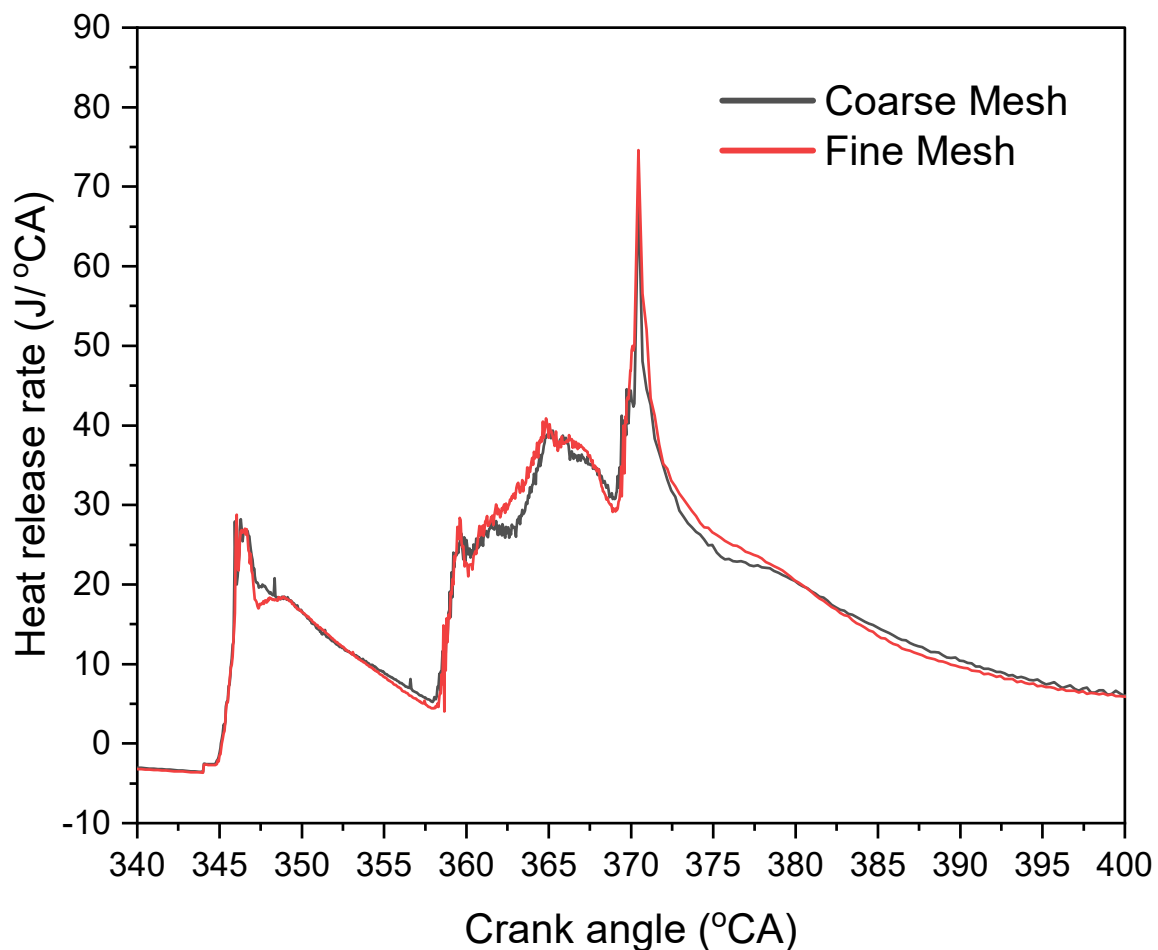

Figure 4. Comparison of HRR using coarse and fine mesh for grid sensitivity analysis.

2.4. Model Validation

The FCC simulation setup was validated against experimental data considering the heat release rate. The purpose of this validation was to examine the in-cylinder combustion behaviour of the modelling setup at constant boundary conditions with respect to the combustion condition of the test engine. The model was validated with a single injection profile (with an injection period between 356 °CA and 376 °CA), similar to the test engine injection. As presented in Figure 5, a similar trend is noted in both the experimental and simulation setup. The trend was observed during the combustion stroke between crank angles of 350 °CA and 400 °CA. The results are validated by adjusting the injection profile with respect to the crank angles. The error percentage between the actual and simulated output was calculated as 3.8%. Though there is some discrepancy in both graphs, the overall error percentage is less than 5%, and the heat release rate trend is good.
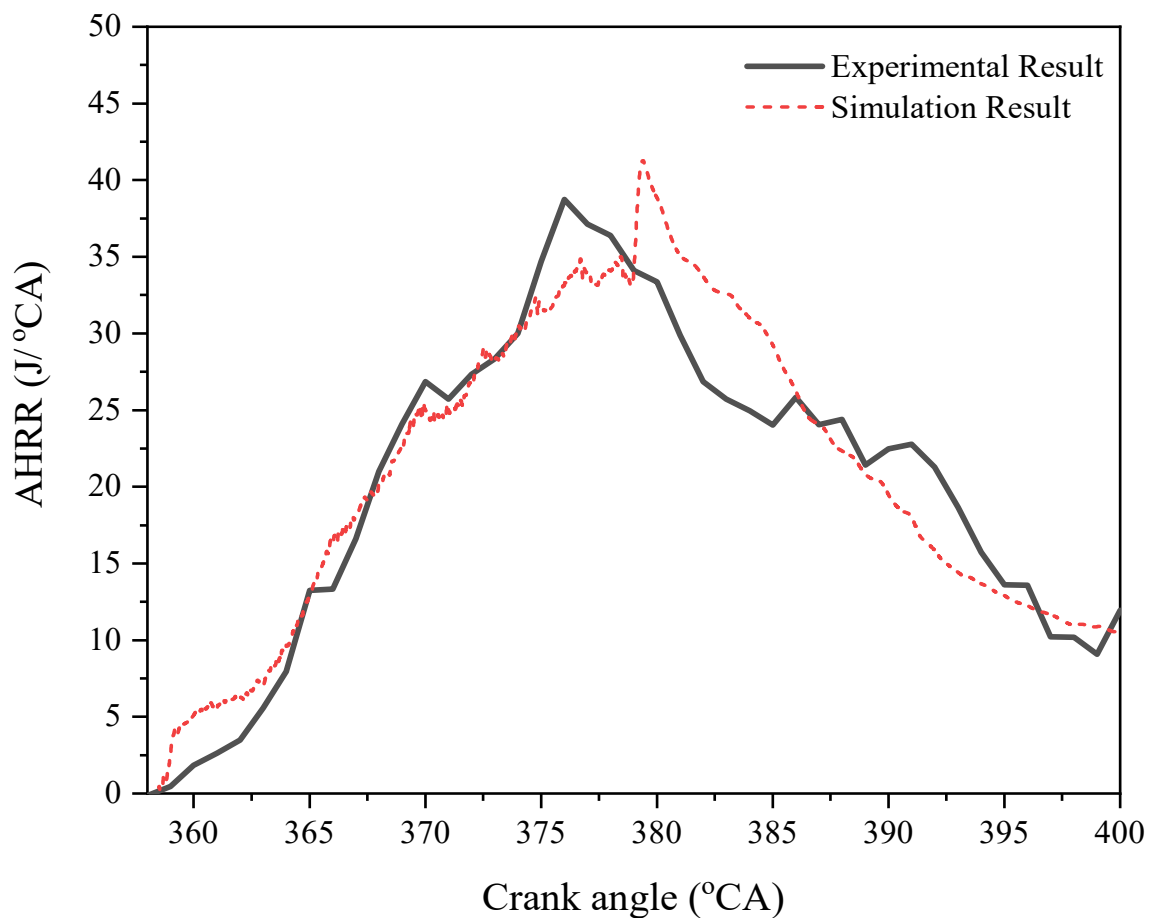

Figure 5. Model validation with experimental HRR result with simulation results.

2.5. Chamber Geometry Modification

As discussed before, the clearance volume of the flat chamber was adjusted by maintaining the same compression ratio and displacement volume to the design of the combustion chambers with respect to the test engine. Bowl geometries such as the double swirl combustion chamber (DSCC), bathtub combustion chamber (BTCC), double toroidal re-entrant combustion chamber (DTRCC), shallow depth combustion chamber (SCC), and stepped bowl combustion chamber (SBCC) were designed as shown in Figure 6. The simulation was carried out for these modified chambers with the simulation steps discussed above by maintaining the same operating parameters and boundary conditions to maintain consistency.
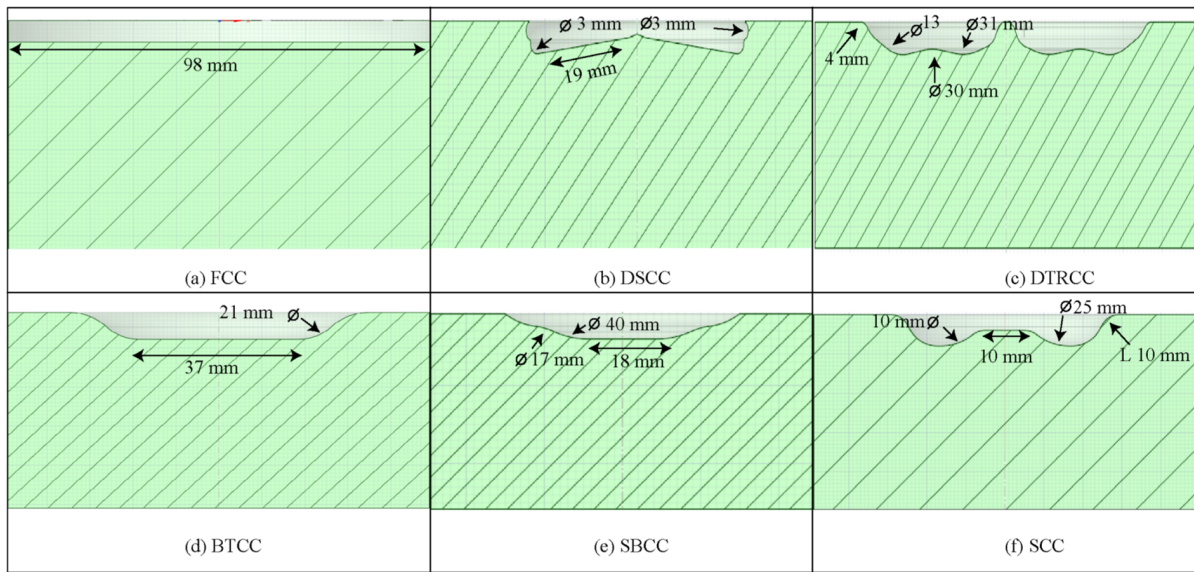
Figure 6. Representation of different piston bowl geometries.

3. Results and Discussions

3.1. Effect of Chamber Modifications on Compression Behaviour

Figure 7 illustrates the temperature distribution of the chamber at the end of the compression stroke at 344 °CA. The results show that varying the bowl shape has a visible impact on the compression rate, which is one of the primary operating parameters for a compression ignition engine. As shown in Figure 7, the SCC (970 K) showed a high-temperature formation than the reference piston FCC (968 K), followed by the SBCC (967 K) and BTCC (966 K). The DTRCC demonstrated inferior temperature formation (748 K to 815 K) during the compression stroke, which may be due to a longer bowl diameter. For the DTRCC, it can be seen from the temperature plots that the crevice region has high-temperature formation, which can cause rapid and poor combustion in crevice regions. Several studies have reported high unburnt hydrocarbons and NO$_x$ emissions when combustion occurs in crevice regions of the chamber [40,41].
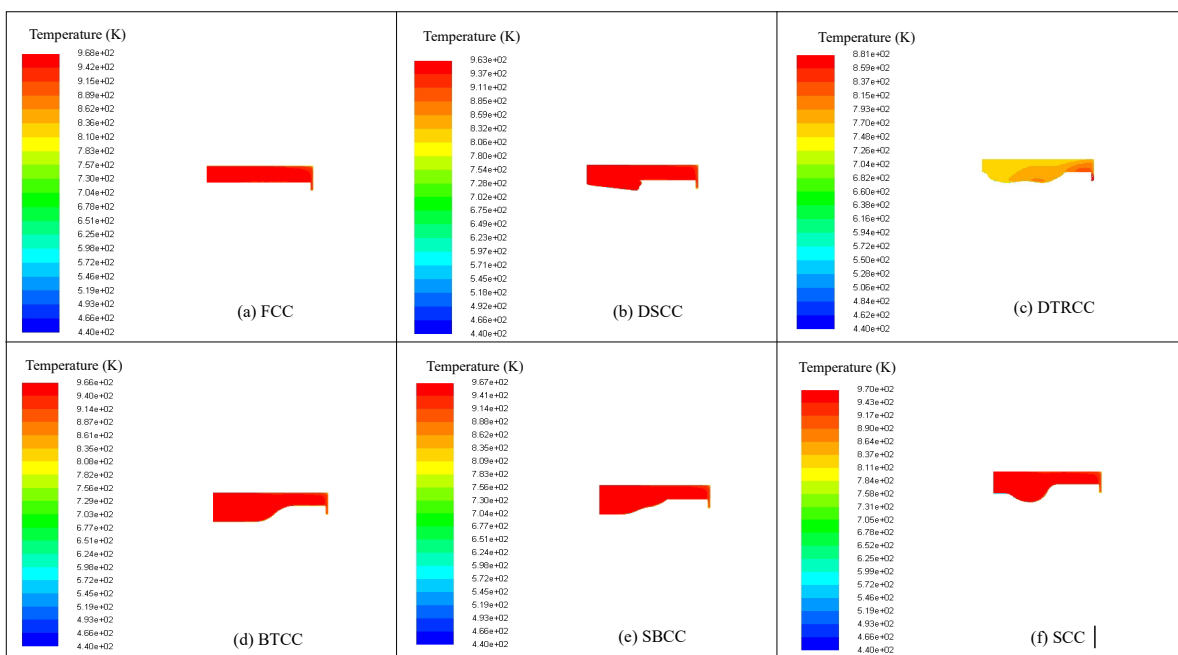

Figure 7. Temperature contours at the end of the compression stroke at 344 °CA.

During the compression stroke, particles become closer together, and the highly inhomogeneous flow of the intake stroke becomes relatively homogeneous during the compression stroke, as shown in Figures 7 and 8 [42]. The velocity distribution of different piston bowl chambers at 344 °CA is illustrated in Figure 8. It is observed from the results that high-velocity rates are formed in the squish region near the cylinder wall. Even though the FCC has no bowl shape, high-velocity motions (8.97 m/s) are observed near the wall region due to surface interactions between the compressed air and moving surfaces of the piston and wall. This phenomenon indicates that the injected air is pushed away from the cylinder axis and makes space for the injected fuel. As predicted, low-velocity rates were observed in the crevice regions as they have very confined spaces. Interestingly, the DTRCC (9.18 m/s) showed high-velocity formation at the end of the compression stroke. Usually, entropy (degree of randomness) should increase under high-temperature conditions; however, compared to the other chambers, the DTRCC formed high-velocity flow motions in the squish region. This is because the DTRCC has less squish space and longer bowl regions; meanwhile, the fluid and wall surface interactions also create high velocities near the wall region. Hence, higher turbulent kinetic energy(TKE) was noticed at the confined squish region. Similar behaviour was also seen in the BTCC (9.24 m/s), with higher TKE than the SCC (9 m/s) because of the shorter squish region.
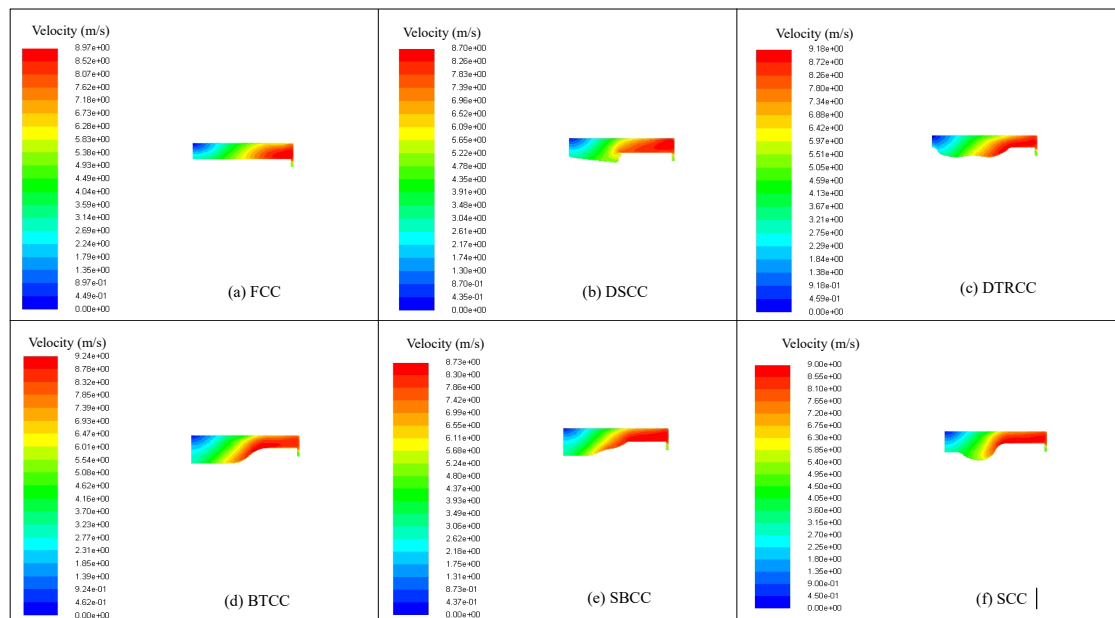

Figure 8. Velocity contours at the end of the compression stroke at 344 °CA.

3.2. Effect of Chamber Modifications on Fuel Particle Distribution

Figure 9 presents the fuel particle distribution with respect to velocity and temperature at 368 °CA during the injection period, which is near the top dead centre (TDC). The DSCC (2170 K) and BTCC (2140 K) showed high-temperature formation rates during the injection period compared with the FCC (2120 K). Due to poor compression rates, the DTRCC showed lower temperature formation at 1990 K compared with other chambers.

To understand fuel dispersion inside the chamber with respect to bowl shape, the temperature and velocity rate of particle traces were analysed. Bowl design signifies fuel distribution and combustion. For instance, in the DSCC and SCC, the fuel is sprayed directly into the bowl region, which restricts the fuel from spreading to the squish and crevice regions. Velocity contours also support that the DSCC and SCC have no particle motions after the bowl region. Targeting the least flow restriction benefits the air–fuel mixture because the loss in spray momentum helps distribute the fuel around the bowl region [43]. A free-flow of particle momentum was noticed with the FCC, DTRCC, BTCC, and SCC due to the absence of complex obstructions to the injected fuel. The results for

these chambers indicate that the injected fuel momentum spreads towards the squish and crevice regions. The distribution rate in the squish region was greater for the FCC and DTRCC due to the absence of hard bowl obstructions. As discussed earlier, accumulated fuels in the crevice and squish regions cause improper combustion and release higher NO_x and UBHC emissions. High-density fuels such as biodiesel have more scope for forming fuel pockets near the crevice regions, making them more susceptible to uniform combustion [44].
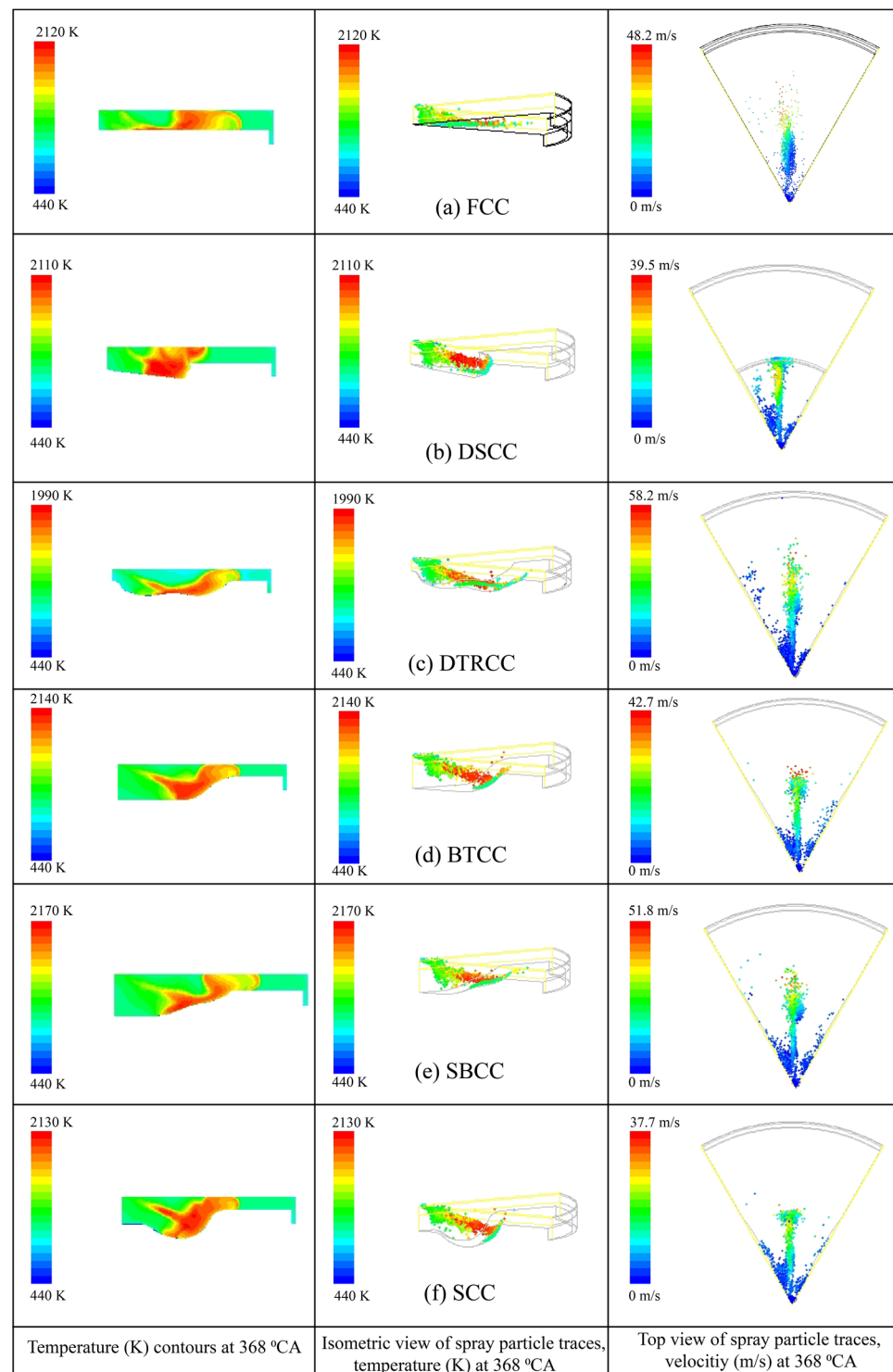
Temperature (K) contours at 368 °CA	Isometric view of spray particle traces, temperature (K) at 368 °CA	Top view of spray particle traces, velocitiy (m/s) at 368 °CA
(a) FCC		
(b) DSCC		
(c) DTRCC		
(d) BTCC		
(e) SBCC		
(f) SCC		

Figure 9. Injection profiles during injection at 368 °CA.

3.3. Effect of Chamber Modifications on In-Cylinder Temperature Distribution

Figures 10 and 11 show the in-cylinder temperature distribution for modified chambers during the middle and end of the combustion stroke at crank angles of 431 °CA and 467 °CA, respectively. As presented in Figures 10 and 11, the chambers with fewer bowl obstructions, such as the FCC and DTRCC, revealed that combustion spreads towards the cylinder wall region with respect to fuel droplet dispersion. Furthermore, because the spray mixture is more prone to hit the walls, it can cause combustion near the wall region. Therefore, there are higher chances for cylinder heat loss as the high-temperature areas are situated alongside the wall. Moreover, compared with other bowl chambers, the FCC and DTRCC showed combustion formation in the crevice regions (Figures 10 and 11). However, the bowl chambers of the DSCC, BTCC, and SCC, showed high-temperature distribution during the combustion stroke, indicating that combustion happened alongside the bowl region. A poor temperature distribution was noted in the DTRCC, where the combustion occurred near the squish region because of the shorter squish area and wider bowl chamber.
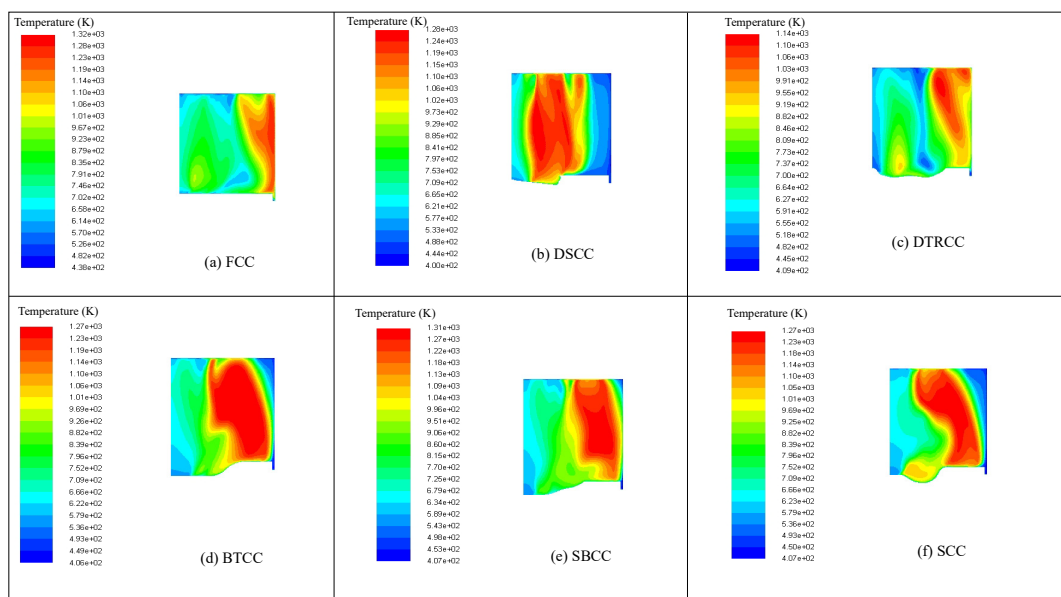

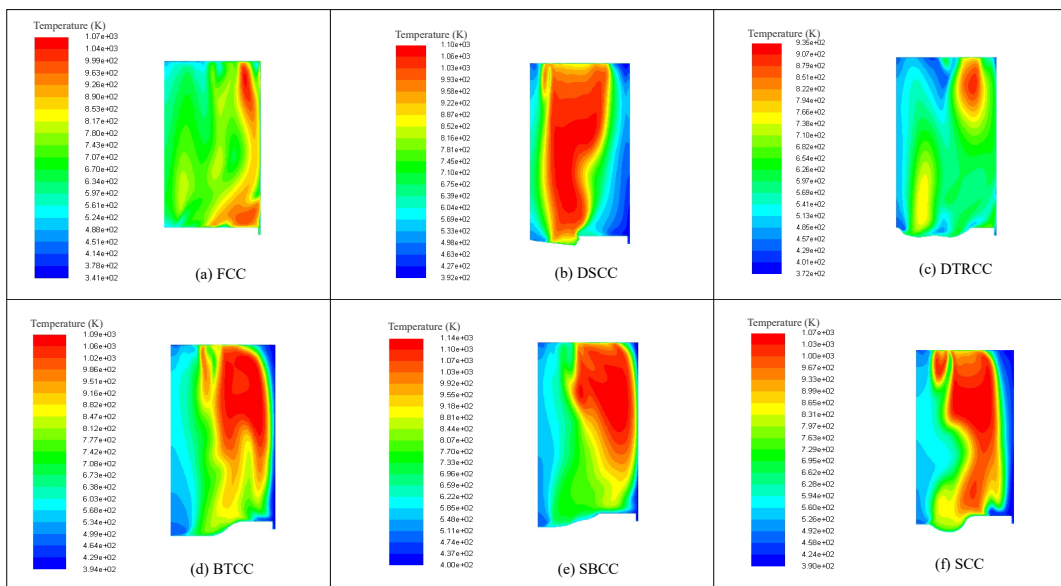**Figure 10.** Temperature contours during the combustion stroke at 431 °CA.

Figure 11. Temperature contours near the BDC at 431 °CA.

Fuel injection is mainly responsible for carrying the combustion near the bowl region. As shown in Figure 9, the injected fuel is dispersed into squish regions for the DTRCC, BTCC, DBCC, and SCC chambers; hence, the combustion plots (Figures 10 and 11) also show combustion at the squish regions of these chambers. Thus, it is concluded from the analysis that in order to conduct combustion with piston bowl geometries, injection type and angle should be adjusted to utilise the bowl region.

3.4. Effect of Chamber Modifications on the In-Cylinder Velocity Distribution

Figures 12 and 13 show velocity distributions at 431 °CA and 467 °CA for different modified chambers. It is observed from the results that higher velocity magnitudes are recorded on top of the piston surface as the piston moves towards the bottom dead centre BDC. Here, the velocity counters represent two main activities: turbulence and piston work [45]. The high velocities situated on the piston head for the SCC (approx. 10.5 m/s) generate significantly more power during the power stroke. In the case of the FCC, the fluid streams dispersed around the piston surface, showing higher velocities than other chambers due to the absence of a bowl region. Furthermore, the DTRCC with a broader bowl exhibited poor velocity distribution due to the formation of less turbulence inside the chamber. Higher magnitude of velocity regimes, 13.9 m/s at 431 °CA and 15 m/s at 497 °CA, were noticed for the DTRCC. However, the irregular velocity stream distribution was recorded for the DSCC due to the uneven turbulence distribution of fluid streams.
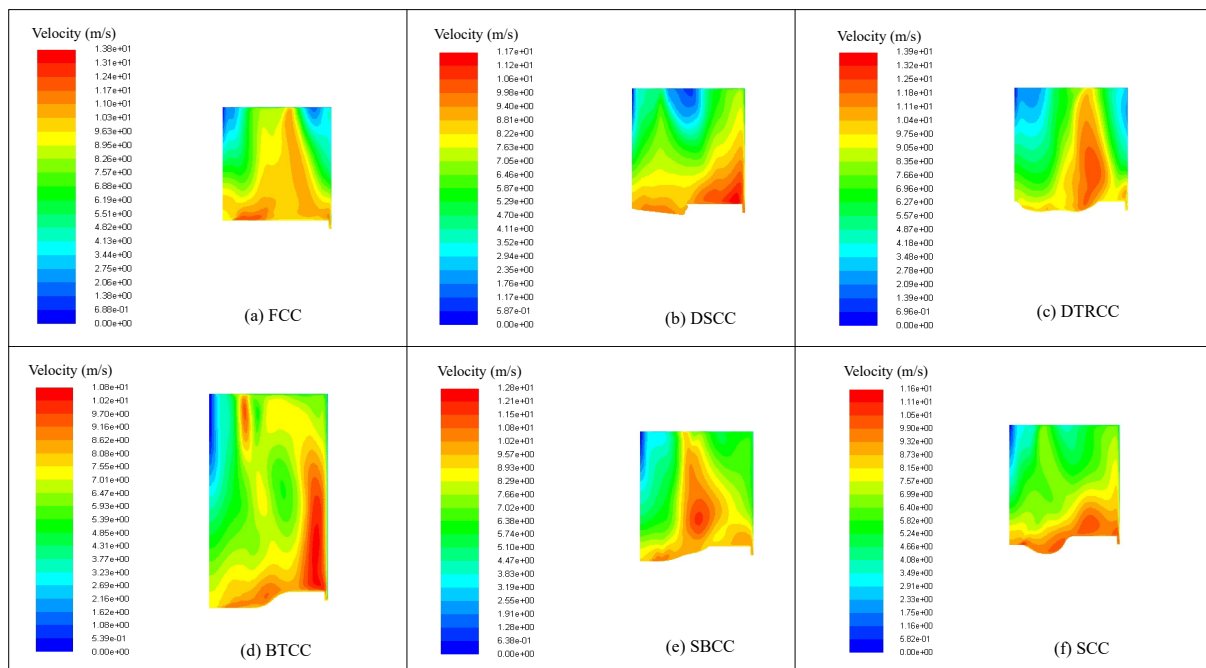

Figure 12. Velocity contours during the combustion stroke at 431 °CA.

3.5. Effect of Chamber Modifications on the Heat Release Rate

The apparent heat release rate (AHRR) for different modified chambers is illustrated in Figure 14. The three humps during the injection were mainly due to the compound HRR caused by multiple split injections. Compared with the reference FCC, all the piston bowl chambers showed high HRRs with pilot injection. This may be due to the increased turbulence rate generated by the piston bowl chambers during the injection stages. The AHRR in the DTRCC was high and more rapid than in the other chambers. However, temperature plots (Figures 10 and 11) and velocity plots (Figures 12 and 13) showed poor combustion rates and spatial distribution within the DTRCC. The main reason for these poor temperatures, velocities, and HRR was uneven and rapid combustion. Furthermore,

as knocking intensity is proportional to peak HRR, the DTRCC is more susceptible to generating knocking under high turbulence conditions.
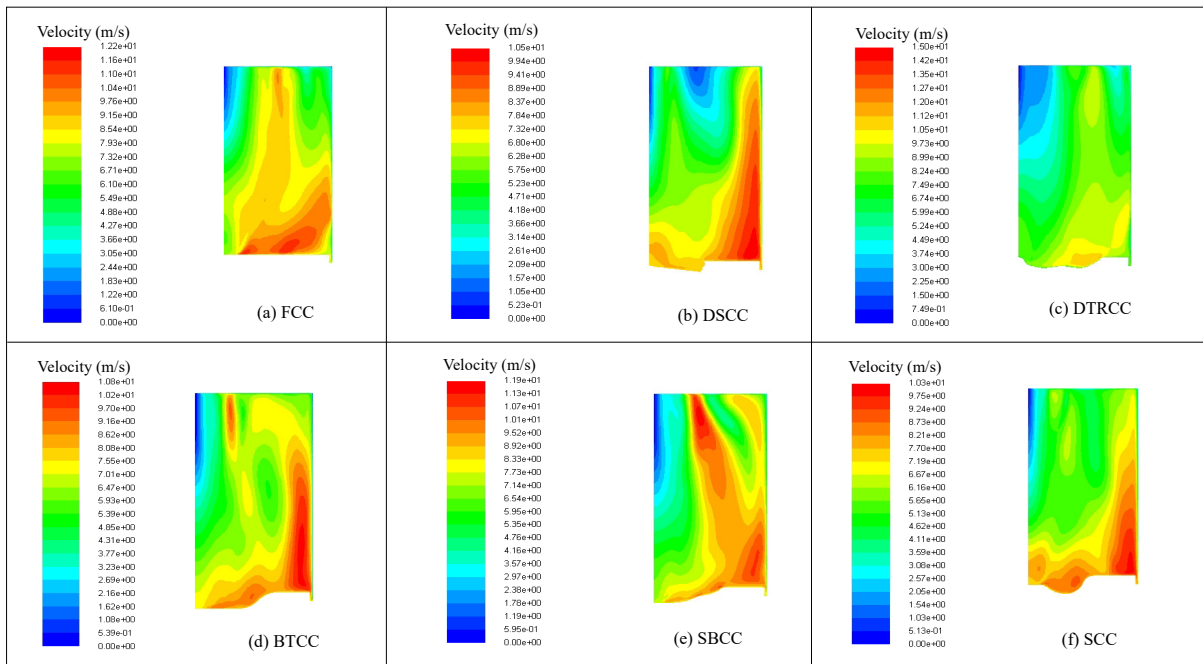

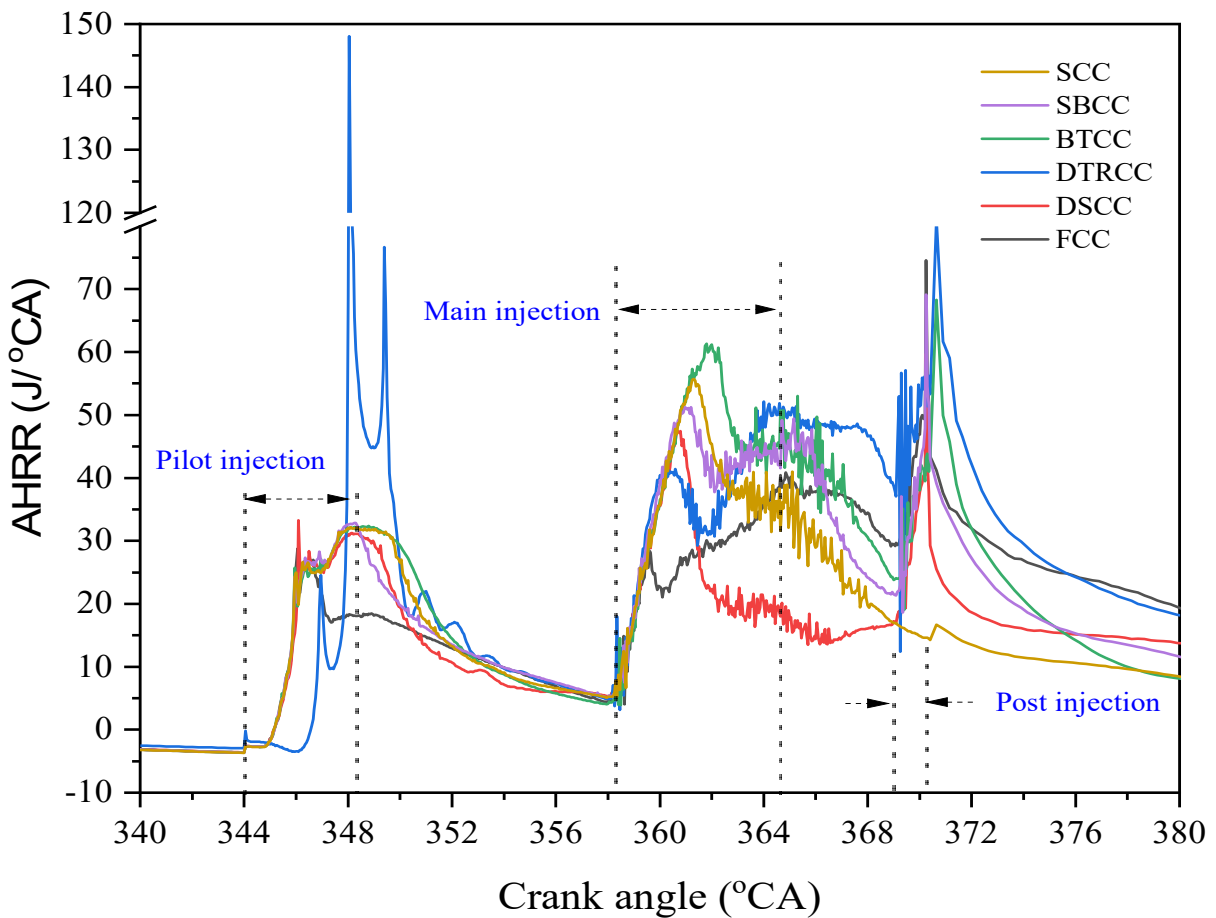**Figure 13.** Velocity contours near the end of the combustion stroke at 431 °CA.

Figure 14. Heat release rate for different piston bowl geometries.

All the chambers showed high AHRRs during the main fuel injection period compared with the FCC. The DSCC and SCC gradually decreased with combustion, suggesting that better fuel combustion occurred with the DSCC and SCC than the BTCC, FCC, SBCC, and DTRCC. During the third injection, the SCC did not record significant variations in the HRR. This may be due to fuel accumulation in the deeper bowl chamber, and suggests that a third post-injection is not required in the SCC chamber model. On the other hand, all the chambers, including the FCC, reacted with the post-injection. Usually, mixture swirling occurs mainly in the bowl region, and it is highly beneficial if the chamber can utilise the squish region. In the case of the DSCC, the injected fuel split towards the bowl and squish area. Thus, the DSCC showed better combustion release rates when compared with other chambers.

3.6. Swirl Ratio and Tumble Ratio

Swirl ratio and tumble ratio greatly influence the air-fuel mixing process. Swirl and tumble flow induce the air flow field, increasing burning rate and TKE. Figure 15 shows the swirl ratio for different piston bowl geometries with respect to crank angles. It is observed that during the suction and compression stroke, swirl ratio is high, then started falling to approximately 0.0 at the end of the compression stroke (380 °CA). Again, during the combustion stroke at 382 °CA to 460 °CA, variation in swirl motions were observed for all the chambers. The DSCC showed a high swirl ratio among all the chambers because of the double swirl bowl chamber, followed by the SCC and BTCC. This clearly indicates that shorter and deeper bowl chambers have higher swirl ratios than longer and shallower bowl chambers (as seen in the SBCC, DTRCC, and FCC).
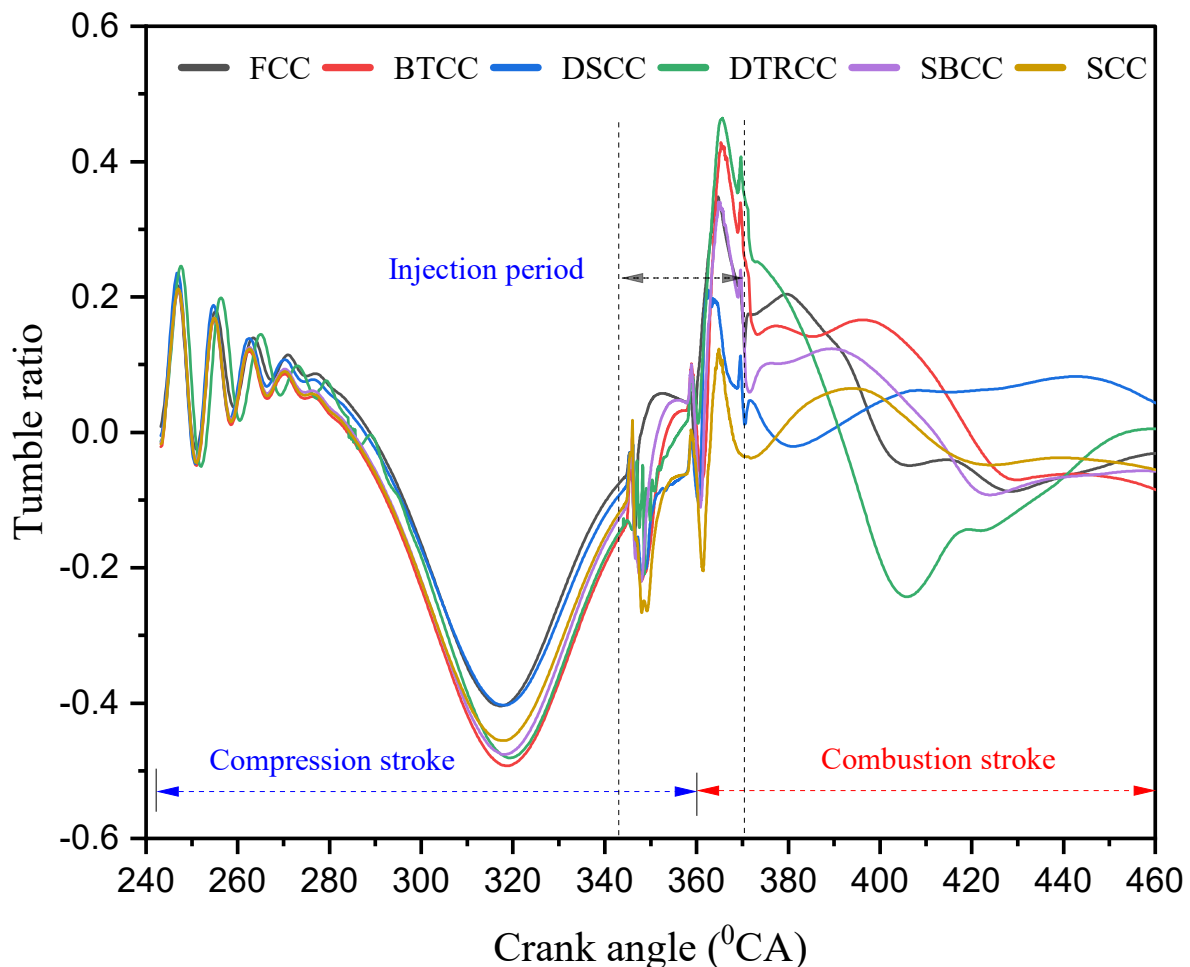

Figure 15. Variation of swirl ratios for different geometries with respect to crank angle.

Figure 16 shows the tumble ratio for different piston bowl geometries with respect to crank angles. The magnitude of the tumble and swirl ratio follows the right-hand rule; hence, the negative ranges in the graphs (Figures 15 and 16) represent the counter-clockwise direction of the flow [46]. When comparing both motions, we observed that the swirl ratio was more dominant in these chambers compared with the tumble ratio. During the suction stroke, near 243 °CA to 280 °CA, variations in tumble motions were observed; meanwhile, during the compression stroke, a negative trend in the tumble ratio was noted. Again, during the combustion stroke, variation in the tumble ratio was seen. For the DTRCC, SBCC, and FCC, a peak tumble ratio was observed over other chambers, which was the opposite of the swirl ratio results. Furthermore, a high tumble ratio was observed during the combustion stroke, whereas a high swirl ratio was observed during the suction stroke.
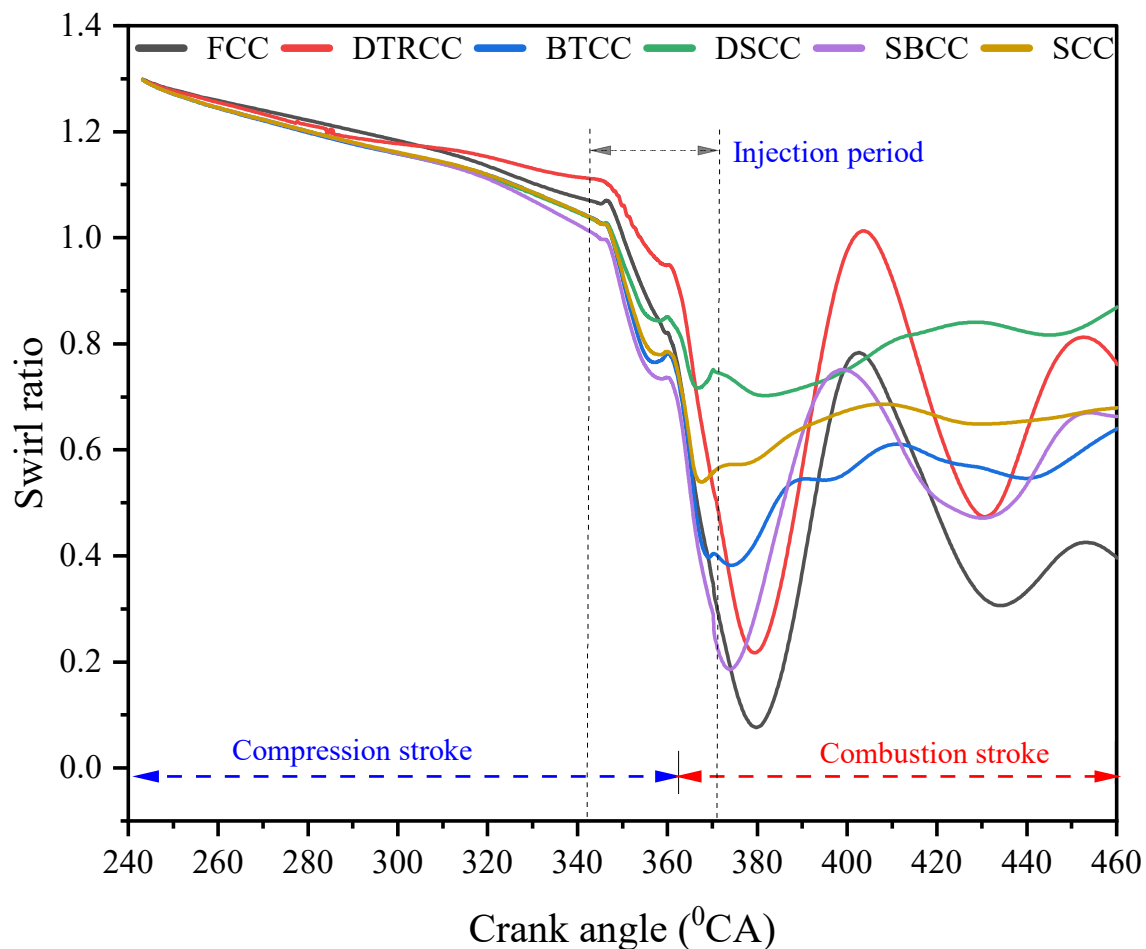

Figure 16. Variation of tumble ratios for different geometries with respect to crank angle.

4. Conclusions and Recommendations

This research paper provides the computational results of DSCC, DTRCC, BTCC, SBCC and SCC geometries and their combustion analysis with respect to the FCC. The conclusions of this study are as follows:

1. The results show that the combustion distribution pattern is quite different among the piston bowl geometries. From the examined velocity profiles, the bowl depth and length affect the spatial distribution of fluid motions inside the cylinder, which causes high-turbulence motions around the chamber.
2. The DSCC (swirl chamber) showed better combustion performance than the other chambers considering the better temperature and velocity distribution, as well as the high swirl ratio and low HRR.

3. The SCC showed better combustion rates, velocity distribution, and HRR compared with the FCC and others, whereas the DTRCC showed poor temperature formation and rapid velocity distribution, which can lead to knocking.
4. A high swirl ratio was observed during the suction stroke, and a high tumble ratio was observed during the combustion stroke, which increased the turbulence rates of the piston bowl geometries.

It is noted that this paper concentrates on the characteristics and behaviour of chamber modifications using simulation results, particularly examining the changes and impact of chamber modifications on combustion. The DSCC has a groove structure that splits the injected fuel into the squish and bowl regions. As the DSCC provided better results, it is recommended to add groove structures to bowl chambers for better combustion. This study shows that fuel injection distribution impacts combustion rates. Furthermore, injected spray plays a controlling role in causing combustion near bowl regions. Hence, one should consider adjusting injection rates and spray patterns when optimising combustion chambers. In addition, emission formation rates of modified chambers need to be tested to examine the role of chamber modifications on emission formations.

Nomenclature

AHRR	Apparent heat release rate
BDC	Bottom dead centre
BTCC	Bathtub combustion chamber
CFD	Computational fluid dynamics
DSCC	Double swirl combustion chamber
DTRCC	Double toroidal re-entrant combustion chamber
FCC	Flat combustion chamber
HCC	Hemispherical combustion chamber
SCC	Shallow depth combustion chamber
SBCC	Stepped bowl combustion chamber
TDC	Top dead centre
TKE	Turbulent kinetic energy
TRCC	Toroidal re-entrant combustion chamber
LSCC	Lateral swirl combustion chamber
LTC	Low-temperature combustion

References

1. Kanda, T.; Hakozaki, T.; Uchimoto, T.; Hatano, J.; Kitayama, N.; Sono, H. PCCI Operation with Early Injection of Conventional Diesel Fuel. *SAE Trans.* **2005**, *114*, 584–593.
2. Praveena, V.; Martin, M.L.J.; Varuvel, E.G. Combined effects of nozzle hole variation and piston bowl geometry modification on performance characteristics of a diesel engine with energy and exergy approach. *J. Clean. Prod.* **2022**, *375*, 133946. [CrossRef]
3. Ashok, B.; Nanthagopal, K.; Saravanan, B.; Azad, K.; Patel, D.; Sudarshan, B.; Ramasamy, R.A. Study on isobutanol and Calophyllum inophyllum biodiesel as a partial replacement in CI engine applications. *Fuel* **2019**, *235*, 984–994. [CrossRef]

4. Azad, A.K.; Adhikari, J.; Halder, P.; Rasul, M.G.; Hassan, N.M.S.; Khan, M.M.K.; Naqvi, S.R.; Viswanathan, K. Performance, Emission and Combustion Characteristics of a Diesel Engine Powered by Macadamia and Grapeseed Biodiesels. *Energies* **2020**, *13*, 2748. [CrossRef]

5. Piano, A.; Roggio, S.; Millo, F.; García, A.; Micó, C.; Lewiski, F.; Pesce, F.; Vassallo, A.; Bianco, A. Numerical and optical soot characterisation through 2-color pyrometry technique for an innovative diesel piston bowl design. *Fuel* **2023**, *333*, 126347. [CrossRef]

6. Soni, D.K.; Gupta, R. Numerical analysis of flow dynamics for two piston bowl designs at different spray angles. *J. Clean. Prod.* **2017**, *149*, 723–734. [CrossRef]

7. Gafoor, C.A.; Gupta, R. Numerical investigation of piston bowl geometry and swirl ratio on emission from diesel engines. *Energy Convers. Manag.* **2015**, *101*, 541–551. [CrossRef]

8. Lawrence, K.R.; Huang, Z.; Nguyen, X.P.; Balasubramanian, D.; Gangula, V.R.; Doddipalli, R.R.; Le, V.V.; Bharathy, S.; Hoang, A.T. Exploration over combined impacts of modified piston bowl geometry and tert-butyl hydroquinone additive-included biodiesel/diesel blend on diesel engine behaviors. *Fuel* **2022**, *322*, 124206. [CrossRef]

9. Azad, A.K.; Rasul, M.; Khan, M.; Sharma, S.; Hazrat, M. Prospect of biofuels as an alternative transport fuel in Australia. *Renew. Sustain. Energy Rev.* **2015**, *43*, 331–351. [CrossRef]

10. Bhuiya, M.M.K.; Rasul, M.; Khan, M.; Ashwath, N.; Azad, A. Prospects of 2nd generation biodiesel as a sustainable fuel—Part: 1 selection of feedstocks, oil extraction techniques and conversion technologies. *Renew. Sustain. Energy Rev.* **2016**, *55*, 1109–1128. [CrossRef]

11. Bhuiya, M.M.K.; Rasul, M.; Khan, M.; Ashwath, N.; Azad, A.; Hazrat, M. Prospects of 2nd generation biodiesel as a sustainable fuel—Part 2: Properties, performance and emission characteristics. *Renew. Sustain. Energy Rev.* **2016**, *55*, 1129–1146. [CrossRef]

12. Mofijur, M.; Rasul, M.G.; Hyde, J.; Azad, A.K.; Mamat, R.; Bhuiya, M.M.K. Role of biofuel and their binary (diesel–biodiesel) and ternary (ethanol–biodiesel–diesel) blends on internal combustion engines emission reduction. *Renew. Sustain. Energy Rev.* **2016**, *53*, 265–278. [CrossRef]

13. Azad, A.; Rasul, M.; Khan, M.; Sharma, S.C.; Islam, R. Prospect of Moringa Seed Oil as a Sustainable Biodiesel Fuel in Australia: A Review. *Procedia Eng.* **2015**, *105*, 601–606. [CrossRef]

14. Azad, A.; Rasul, M.; Khan, M.; Sharma, S.C.; Mofijur, M.; Bhuiya, M. Prospects, feedstocks and challenges of biodiesel production from beauty leaf oil and castor oil: A nonedible oil sources in Australia. *Renew. Sustain. Energy Rev.* **2016**, *61*, 302–318. [CrossRef]

15. Bhuiya, M.; Rasul, M.; Khan, M.; Ashwath, N.; Azad, A.; Hazrat, M. Second Generation Biodiesel: Potential Alternative to-edible Oil-derived Biodiesel. *Energy Procedia* **2014**, *61*, 1969–1972. [CrossRef]

16. Halder, P.; Azad, K.; Shah, S.; Sarker, E. 8—Prospects and technological advancement of cellulosic bioethanol ecofuel production. In *Advances in Eco-Fuels for a Sustainable Environment*; Azad, K., Ed.; Woodhead Publishing: Cambridge, UK, 2019; pp. 211–236.

17. Uddin, S.A.; Azad, A.; Alam, M.; Ahamed, J. Performance of a Diesel Engine Run with Mustard-Kerosene Blends. *Procedia Eng.* **2015**, *105*, 698–704. [CrossRef]

18. Jaichandar, S.; Annamalai, K. Effects of open combustion chamber geometries on the performance of pongamia biodiesel in a DI diesel engine. *Fuel* **2012**, *98*, 272–279. [CrossRef]

19. Jaichandar, S.; Annamalai, K. Influences of re-entrant combustion chamber geometry on the performance of Pongamia biodiesel in a DI diesel engine. *Energy* **2012**, *44*, 633–640. [CrossRef]

20. Jaichandar, S.; Kumar, P.S.; Annamalai, K. Combined effect of injection timing and combustion chamber geometry on the performance of a biodiesel fueled diesel engine. *Energy* **2012**, *47*, 388–394. [CrossRef]

21. Channappagoudra, M.; Ramesh, K.; Manavendra, G. Comparative study of standard engine and modified engine with different piston bowl geometries operated with B20 fuel blend. *Renew. Energy* **2019**, *133*, 216–232. [CrossRef]

22. Pastor, J.V.; García, A.; Micó, C.; Lewiski, F.; Vassallo, A.; Pesce, F. Effect of a novel piston geometry on the combustion process of a light-duty compression ignition engine: An optical analysis. *Energy* **2021**, *221*, 119764. [CrossRef]

23. Li, X.; Zhou, H.; Zhao, L.M.; Su, L.; Xu, H.; Liu, F. Effect of split injections coupled with swirl on combustion performance in DI diesel engines. *Energy Convers. Manag.* **2016**, *129*, 180–188. [CrossRef]

24. Li, X.; Chen, Y.; Su, L.; Liu, F. Effects of lateral swirl combustion chamber geometries on the combustion and emission characteristics of DI diesel engines and a matching method for the combustion chamber geometry. *Fuel* **2018**, *224*, 644–660. [CrossRef]

25. Cao, L.; Bhave, A.; Su, H.; Mosbach, S.; Kraft, M.; Dris, A.; McDavid, R.M. Influence of Injection Timing and Piston Bowl Geometry on PCCI Combustion and Emissions. *SAE Int. J. Engines* **2009**, *2*, 1019–1033. [CrossRef]

26. Xu, L.; Bai, X.-S.; Li, Y.; Treacy, M.; Li, C.; Tunestål, P.; Tunér, M.; Lu, X. Effect of piston bowl geometry and compression ratio on in-cylinder combustion and engine performance in a gasoline direct-injection compression ignition engine under different injection conditions. *Appl. Energy* **2020**, *280*, 115920. [CrossRef]

27. Lee, S.; Park, S. Optimization of the piston bowl geometry and the operating conditions of a gasoline-diesel dual-fuel engine based on a compression ignition engine. *Energy* **2017**, *121*, 433–448. [CrossRef]

28. Shen, Z.; Wang, X.; Zhao, H.; Lin, B.; Shen, Y.; Yang, J. Numerical investigation of natural gas-diesel dual-fuel engine with different piston geometries and radial clearances. *Energy* **2021**, *220*, 119706. [CrossRef]

29. Han, S.; Kim, J.; Bae, C. Effect of air–fuel mixing quality on characteristics of conventional and low temperature diesel combustion. *Appl. Energy* **2014**, *119*, 454–466. [CrossRef]

30. Hao, C.; Zhang, Z.; Wang, Z.; Bai, H.; Li, Y.; Li, Y.; Lu, Z. Investigation of spray angle and combustion chamber geometry to improve combustion performance at full load on a heavy-duty diesel engine using genetic algorithm. *Energy Convers. Manag.* **2022**, *267*, 115862. [CrossRef]
31. Saito, T.; Daisho, Y.; Uchida, N.; Ikeya, N. Effects of Combustion Chamber Geometry on Diesel Combustion. *SAE Trans.* **1986**, *95*, 793–803.
32. Varun; Singh, P.; Tiwari, S.K.; Singh, R.; Kumar, N. Modification in combustion chamber geometry of CI engines for suitability of biodiesel: A review. *Renew. Sustain. Energy Rev.* **2017**, *79*, 1016–1033. [CrossRef]
33. Venu, H.; Raju, V.D.; Subramani, L. Combined effect of influence of nano additives, combustion chamber geometry and injection timing in a DI diesel engine fuelled with ternary (diesel-biodiesel-ethanol) blends. *Energy* **2019**, *174*, 386–406. [CrossRef]
34. Krishnaraj, J.; Vasanthakumar, P.; Hariharan, J.; Vinoth, T.; Karthikayan, S. Combustion Simulation and Emission Prediction of Different Combustion Chamber Geometries Using Finite Element Method. *Mater. Today Proc.* **2017**, *4*, 7903–7910. [CrossRef]
35. Bapu, B.R.; Saravanakumar, L.; Prasad, B.D. Effects of combustion chamber geometry on combustion characteristics of a DI diesel engine fueled with calophyllum inophyllum methyl ester. *J. Energy Inst.* **2017**, *90*, 82–100. [CrossRef]
36. Hazrat, M.A.; Rasul, M.G.; Mofijur, M.; Khan, M.M.K.; Djavanroodi, F.; Azad, A.K.; Bhuiya, M.M.K.; Silitonga, A. A Mini Review on the Cold Flow Properties of Biodiesel and its Blends. *Front. Energy Res.* **2020**, *8*, 598651. [CrossRef]
37. Azad, A.K.; Rasul, M.G.; Khan, M.M.K.; Sharma, S.C.; Bhuiya, M.M.K. Recent development of biodiesel combustion strategies and modelling for compression ignition engines. *Renew. Sustain. Energy Rev.* **2016**, *56*, 1068–1086. [CrossRef]
38. Varol, Y.; Oztop, H.F.; Firat, M.; Koca, A. CFD modeling of heat transfer and fluid flow inside a pent-roof type combustion chamber using dynamic model. *Int. Commun. Heat Mass Transf.* **2010**, *37*, 1366–1375. [CrossRef]
39. Han, Z.; Reitz, R.D. Turbulence modeling of internal combustion engines using RNG κ-ε models. *Combust. Sci. Technol.* **1995**, *106*, 267–295. [CrossRef]
40. Duan, X.; Zhang, S.; Liu, Y.; Li, Y.; Liu, J.; Lai, M.-C.; Deng, B. Numerical investigation the effects of the twin-spark plugs coupled with EGR on the combustion process and emissions characteristics in a lean burn natural gas SI engine. *Energy* **2020**, *206*, 118181. [CrossRef]
41. Li, J.; Yang, W.; An, H.; Maghbouli, A.; Chou, S. Effects of piston bowl geometry on combustion and emission characteristics of biodiesel fueled diesel engines. *Fuel* **2014**, *120*, 66–73. [CrossRef]
42. Banaeizadeh, A.; Afshari, A.; Schock, H.; Jaberi, F. Large-eddy simulations of turbulent flows in internal combustion engines. *Int. J. Heat Mass Transf.* **2013**, *60*, 781–796. [CrossRef]
43. Yadav, J.; Venkatesh, P.; Pischinger, S. Application of micro-genetic algorithms to optimise piston bowl geometries for heavy-duty engines running on diesel and 1-Octanol fuels. *Appl. Therm. Eng.* **2023**, *226*, 120236. [CrossRef]
44. Doppalapudi, A.; Azad, A.; Khan, M. Advanced strategies to reduce harmful nitrogen-oxide emissions from biodiesel fueled engine. *Renew. Sustain. Energy Rev.* **2023**, *174*, 113123. [CrossRef]
45. Doppalapudi, A.; Azad, A.; Khan, M. Combustion chamber modifications to improve diesel engine performance and reduce emissions: A review. *Renew. Sustain. Energy Rev.* **2021**, *152*, 111683. [CrossRef]
46. Lee, K.; Bae, C.; Kang, K. The effects of tumble and swirl flows on flame propagation in a four-valve S.I. engine. *Appl. Therm. Eng.* **2007**, *27*, 2122–2130. [CrossRef]